Research Article | Vol. 29, No. 13 / 21 June 2021 / Optics Express 20275
Optics EXPRESS

Broadband long-wave infrared metamaterial absorber based on single-sized cut-wire resonators

ZHENG QIN,[1,2] DEJIA MENG,[1,5] FUMING YANG,[1,2] XIAOYAN SHI,[1,2] ZHONGZHU LIANG,[1,2,3,6] HAIYANG XU,[3] DAVID R. SMITH,[4] AND YICHUN LIU[3]

[1]State Key Laboratory of Applied Optics, Changchun Institute of Optics, Fine Mechanics and Physics, Chinese Academy of Sciences, Changchun, Jilin 130033, China
[2]University of the Chinese Academy of Sciences, China
[3]Center for Advanced Optoelectronic Functional Materials Research and Key Laboratory of UV Light-Emitting Materials and Technology of Ministry of Education, College of Physics, Northeast Normal University, Changchun 130024, China
[4]Center for Metamaterials and Integrated Plasmonics, Duke University, P.O. Box 90291, Durham, North Carolina 27708, USA
[5]djmeng@sklao.ac.cn
[6]liangzz@nenu.edu.cn

Abstract: Broadband absorption is critical for the applications of metamaterial absorbers. In this work, a broadband long-wave infrared (LWIR) absorber with classical metal-dielectric-metal configuration is numerically demonstrated. The absorber consists of single-sized cut-wire arrays that show broadband and high extinction ratio, attributed to polarization-selective simultaneous excitation of propagated and localized surface plasmon resonances. The average absorption rate of the TM wave reaches 91.7% and 90% of the incident light is absorbed by the resonator in the wavelength range of 7.5–13.25μm so that the average extinction ratio in the resonator layer reaches 125. The polarization insensitive broadband absorption can be obtained by a cross resonator which can be treated as a pair of cut-wires perpendicular to each other. Our metamaterial absorber with single-sized resonators shows spatially concentrated broadband absorption and may have promising applications for hot-electron devices, infrared imaging, and thermal detection.

1. Introduction

Metamaterial absorbers (MAs) can confine and completely absorb incident electromagnetic wave to the subwavelength scale [1], have promising applications in detection [2–4], thermal emitters [5,6], energy harvesting [7,8], cooling [9,10], and so on. The working wavelength of the MAs can be manipulated by its geometric parameters [1]. Therefore, the geometric configuration of the metamaterial structure can be designed to achieve perfect absorption at the non-absorption wavelength of natural materials. MAs based on metal-dielectric-metal sandwich structure is gradually realized in the microwave [11], terahertz [12], infrared [1,13], and visible light [14] and are used in gas detection [15,16], solar energy collection [17–19], imaging [20–23], invisible cloaks [24], etc. in these domains, broadband strong absorption is critical for the performance [22].

Since the general MA has only one perfect absorption peak [1,11], extensive research has focused on achieving multiband or broadband absorption [7,25,26]. In the infrared band, the general strategy to increase the absorption bandwidth is to use a supercell configuration that integrates multiple coplanar resonators [19,27,28] such as multiple sizes of crosses, disks, and ellipses, to obtain multiple localized surface plasmon resonances (LSPRs). The performance of

#430068 https://doi.org/10.1364/OE.430068
Journal © 2021 Received 28 Apr 2021; revised 2 Jun 2021; accepted 4 Jun 2021; published 14 Jun 2021

Optics EXPRESS

the absorber is limited by the number of resonators and the coupling effect between adjacent resonators. Pyramidal metal-dielectric multilayer structure [25,29–33] is another strategy and the absorption bandwidth can be extended by increasing the number of stacked layers, which is also more convenient in design. For example, broadband absorption is achieved by stacking multiple layers of Au-SiO_2 [25]. However, the increase in the number of layers raises the requirements of the manufacturing process, not only the number of preparation steps increases, but the requirements for accuracy will also increase due to the increase in the number of layers. To achieve broadband absorption with a simple structure, some dielectric materials with high intrinsic absorption are used in the design of MAs, such as silicon nitride [26], silicon dioxide [10], aluminum oxide [34], etc. Broadband or dual-band absorption can be obtained due to the enhanced intrinsic absorption of the material by the surface plasmon resonances (SPRs). However, the absorption bandwidth is limited by the inherent parameters of the material, and the strong dispersion of the material limits the application of the absorber. In contrast, by selecting appropriate metal and structural parameters to excite multiple resonance modes, multi-peaks or broadband absorption can be obtained [3,35,36]. For example, Fei Ding et al. used a titanium disk to simultaneously excite LSPRs and propagated surface plasmon resonances (PSPRs) to obtain broadband absorption in the near-infrared band [37]. On the other hand, in recent years, polarization detection and polarization imaging have gradually become research hotspots [38]. However, most of the previous broadband absorbers only focused on realizing polarization-insensitive absorption. There are few studies on polarization-sensitive or polarization-selective absorbers. The general solution to achieve polarization selective absorption uses a one-dimensional grating structure. Although a high extinction ratio can be achieved, the absorption bandwidth is limited [39,40]. Therefore, long-wave infrared absorbers with high polarization selection ratio and broadband absorption are rarely studied. Besides, some applications such as microbolometers and hot-electron collection devices require not only perfect absorption but also spatially concentrated absorption [41,42]. In hot-electron devices, the incident light couples with the resonator to excite surface plasmon resonators (SPRs), generate local hot spots at the metal-silicon interface so that the electrons obtain sufficient energy to transfer across the Schottky barrier at the metal-semiconductor interface to form a photocurrent [42]. As far as we know, the hot-electron devices with MAs are limited by the narrow working band. In the past absorber design, broadband and spatially concentrated absorption seem to be contradictory [33,43], the incident light of different wavelengths is absorbed by different resonators or different compositions of absorbers. Therefore, it is still a challenge to use a simple configuration to simultaneously achieve broadband, spatially concentrated, polarization insensitive and incident angle insensitive absorption.

In this work, we proposed a long-wave infrared broadband absorber design with a simple configuration. Polarization selective absorption, spatially concentrated absorption, polarization insensitive and incident angle insensitive absorption are achieved respectively by reasonably manipulated the configuration of the MA. First, we proposed a titanium-silicon-titanium (Ti-Si-Ti) absorber configuration with cut-wire arrays, which realized the broadband absorption of TM wave and single-peak absorption of TE wave. The physical mechanism of the broadband absorption of TM wave is attributed to simultaneous exciting of PSPR and LSPR, and the absorption of TE wave is due to the cavity mode. Next, the absorption of the TE wave is suppressed by using an aluminum bottom and, a polarization selective broadband absorption is obtained. More than 90% of the incident TM wave was confined in the resonator and converted into heat and only a few of TE wave was absorbed by the bottom, so we obtained high extinction ratio reached 125. Finally, we use a cross-shaped resonator with 90° rotational symmetry to obtain polarization insensitive, incident angle insensitive and spatially concentrated broadband absorption. The average absorption rate of the absorber in the wavelength range of 7.5~13.25μm reaches 94% under normal incidence. The absorber exhibits insensitivity to polarization and incident angle,

Optics EXPRESS

almost all of the incident waves absorbed by the resonator as well. The absorber we designed can be used for infrared imaging, thermal detection, thermal electron collection.

2. Result and discussion

2.1. Polarization-dependent broadband-single tunable wavelength absorber

As shown in Fig. 1(a), The MA is composed of an array of cut-wire resonators and a plane bottom, separated by a dielectric layer. The geometric parameters of the absorber include the period, the thickness of the resonator, the thickness of the bottom, the thickness of the dielectric layer, and the length and width of the resonator, indicated by P, t, t_b, d, L, and w, respectively. We set the geometric parameters of the absorber as P = 1.6 μm, L = 1.2 μm, w = 0.2 μm, t = 60 nm, d = 650 nm, and t_b = 200 nm. To verify the absorber performance, we performed a simulation using the Finite Difference Time Domain method. The material parameters of titanium and silicon were obtained from Rakić [44] and Palik [45], respectively. The absorber performance was calculated using $A(\lambda) = 1 - R(\lambda)$ since the titanium bottom was sufficiently thick to block the incident light in the simulation range. As shown in Fig. 1(a), the polarization angle of incident light under normal incidence is defined as the angle between the incident electric field component and the x-axis.

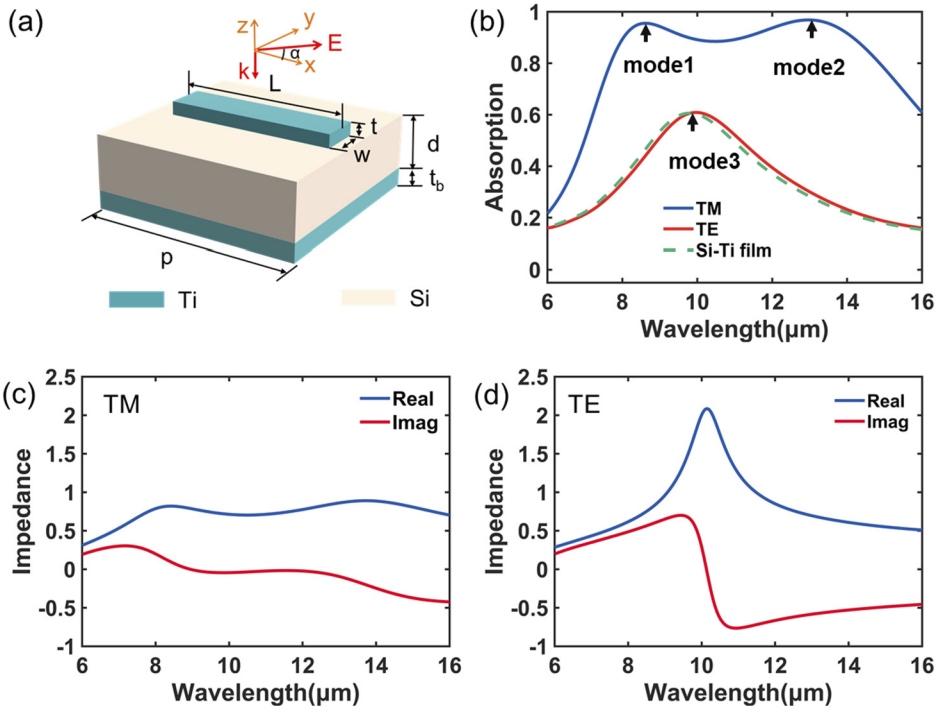

Fig. 1. Schematic diagram of the structure of the metamaterial absorber, which consists of a titanium bottom and titanium resonator array separated by a dielectric layer. Its geometric parameters are: P = 1.6μm, L=1.2μm, w=0.2μm, t=60 nm, d=650 nm, t_b=200 nm. (b) The absorption spectrum of the absorber under TM and TE incidence and the absorption spectrum of the Si-Ti film (c) The impedance of the absorber structure when TM wave is incident. (d) Impedance of the absorber structure under TE wave incident

The performance of the MA is shown in Fig. 1(b). When the polarization angle is 0°(TM), the incident electric field is parallel to the cut-wire resonator. At this time, the absorber has two

Optics EXPRESS

obvious absorption peaks in the simulated wavelength band (Fig. 1(b) blue solid line), respectively located at 8.6μm and 12.9μm, expressed as mode1 and mode2. The absorption rates at mode1 and mode2 reached 95.4% and 97.2%, respectively. The average absorption rate in the wavelength range of 8~14μm reached 92.2%. Besides, when the polarization angle of the incident light gradually increases and is perpendicular to the long axis of the resonator, the two absorption peaks gradually decrease and disappear. When the polarization angle reaches 90°(TE), there is only one absorption peak (green solid line in Fig. 1(b)), which is located at 9.9μm, denoted by mode3 and the absorption rate is 60.9%. That is, the MA can change from broadband absorption to narrowband absorption by changing the polarization direction of incident light. To explain the mechanism of polarization-dependent absorption, we calculated the equivalent impedance of the absorber by [46]:

$$Z = \sqrt{\frac{(1+S_{11})^2 - S_{21}^2}{(1-S_{11})^2 - S_{21}^2}} \tag{1}$$

Here $Z = Z' + iZ''$. The equivalent impedance is calculated from the scattering parameters, and the impedance of air is considered to be $Z_{air} = 1$. The real and imaginary parts of the equivalent impedance both contribute to the reflectivity of the absorber, according to $R = \frac{(Z'-1)^2+(Z'')^2}{(Z'+1)^2+(Z'')^2}$ [46]. Perfect absorption occurs at the wavelength where the equivalent impedance is perfectly matched to air. As shown in Fig. 1(c), when the TM wave is incident, the absorber's impedance matches with the air in a wide waveband. The impedances at the two absorption peaks are Z_1=0.82+i0.08 and Z_2=0.86-i0.08, which are very close to the impedance of air. Here, the slight deviation between the impedance at the two absorption peaks and the air impedance is indicated in the absorption spectrum as the absorption rate does not reach 100%. On the other hand, when the TE wave (the incident electric field is perpendicular to the cut-wire resonator) incident, as is shown in Fig. 1(d), the absorber does not match impedance in the simulated waveband. Although the imaginary part of the impedance is zero at the wavelength of 9.9 μm, the real part reached 2. Therefore, as is shown in Fig. 1(b), only one absorption peak with an absorption rate of 60% is obtained (red solid line).

To further understand the physical mechanism of the broadband absorption of TM wave and single-peak absorption of TE wave, we calculated the magnetic field distribution at the three absorption peaks. As shown in Fig. 2(a), the magnetic field at the absorption peak mode1 is mainly concentrated on the upper and lower surfaces of the resonator, and the dielectric-bottom interface on both sides of the resonator shows the characteristics of PSPR. The influence of the geometric parameters of the absorber on its PSPR can be expressed as [47]:

$$k_{SP} = k_0 \sin\theta + i \times \frac{2\pi}{P} \tag{2}$$

At mode2, the magnetic field is mainly concentrated on the upper and lower surfaces of the resonator and the dielectric cavity below the resonator, showing the characteristics of LSPR, and the resonance can be explained by the LC circuit model [48]:

$$\lambda = 2\pi\sqrt{LC/2} \tag{3}$$

Here, $L = L_r + L_b$, L_r is the kinetic inductance of the resonator and L_b is the kinetic inductance of the bottom. $C = C_e + C_n$, C_e is the capacitance of the adjacent resonators and C_n is the capacitance between two parallel plates sandwiched by the dielectric spacer. Therefore, the broadband absorption of the absorber in the case of TM wave incidence is obtained by the hybrid mode of PSPR and LSPR excited by the resonator array. That is, the incident light coupled to the resonator array so that the incident electric and magnetic fields are concentrated inside

Optics EXPRESS

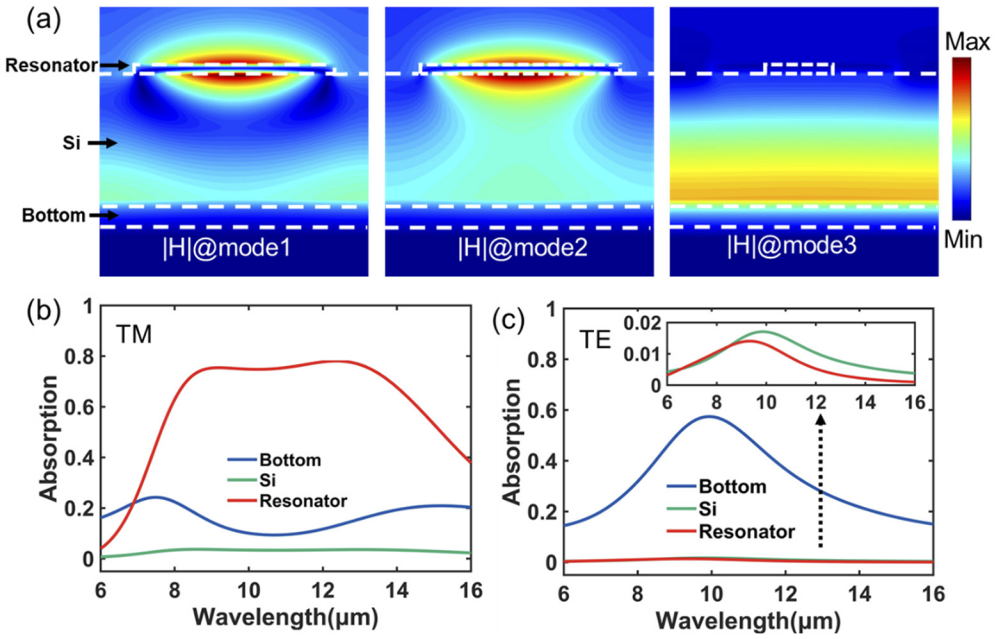

Fig. 2. (a) The magnetic field distribution at the absorption peak, from left to right are mode1, mode2, and mdoe3 respectively. (b) The absorption of each component of the absorber under the incident TM wave, and (c) the incident TE wave, the inset is enlarged view of the absorption spectrum for the bottom and Si

the absorber structure, and the resulting surface current causes ohmic loss of the metal. We calculated the absorption of incident light energy by each layer, through the equation [13]:

$$Q(\omega) = \frac{1}{2} \times \omega \times \varepsilon'' \times |E(\omega)|^2 \tag{4}$$

Here, ω is the angular frequency, ε'' is the imaginary part of the permittivity of the material, and $E(\omega)$ represents the electric-field strength corresponding to angular frequency ω. The normalized result is shown in Fig. 2(b). It can be seen that the energy of the incident light is mainly absorbed by the resonator and the bottom. In the 8~14μm waveband, the absorption contribution of the resonator reaches 70%, absorption contribution of the dielectric layer is less than 2%. The absorption of the bottom layer at the short wave and long wave has increased, we attribute it to the intrinsic absorption of titanium.

Unlike the conditions of TM wave incidence, the magnetic field is uniformly distributed at the interface of the dielectric-metal bottom in the case of TE wave incidence. It shows that the resonator has no surface plasmon response in the simulated waveband, and the absorption peak at this time is caused by the cavity mode from the Si-Ti film. The resonance of the Si-Ti film can be expressed as [49]:

$$d = \frac{\lambda}{2\pi n_d} \tan^{-1}\left(n_d \sqrt{\frac{n_m - n_d}{n_0(n_d^2 - n_0 n_m)}}\right) \tag{5}$$

$$\sqrt{n_m} < n_d \le \sqrt{n_0\left(\frac{k_m^2}{n_m - n_0} + n_m\right)} \tag{6}$$

Here d is the thickness of the dielectric layer, n_0, n_d the real parts of the refractive index of air and the dielectric layer respectively. n_m and k_m are the real and imaginary parts of the complex

Optics EXPRESS

refractive index of the bottom metal. When $n_d = \sqrt{n_0\left(\frac{k_m^2}{n_m - n_0} + n_m\right)}$,a perfect absorption can be obtained. As shown in Fig. 1(b), we calculated the absorption spectrum (green dashed line) of the Si-Ti cavity, at the wavelength of 9.9μm, $\sqrt{n_0\left(\frac{k_m^2}{n_m - n_0} + n_m\right)} = 7.17 > 3.422$, so absorption rate of only 60% is obtained. The absorption spectrum of the Si-Ti film coincides with the absorption spectrum (red solid line) of the TE wave. Therefore, in the case of the TE wave incident, the role of the resonator in the simulated waveband is negligible. The incident light is reflected multiple times in the cavity composed of Air-Si-Ti and absorbed by the underlying titanium.

2.2. Polarization selective spatially concentrated broadband absorber

In some applications, such as polarization detection, it is often required that one polarization direction is perfectly absorbed while the other polarization is absorbed as little as possible. On the other hand, in hot-electron devices, it is often required that the energy of incident light be concentrated at the resonator-dielectric layer interface to generate enough hot electrons. To obtain better polarization selectivity and more spatially concentrated broadband absorption, we replaced the titanium bottom with aluminum which has a lower loss in the long-wave infrared band. The absorption spectrum of the new absorber depends on the polarization angle is shown in Fig. 3(a). It can be seen that the Ti-Si-Al configuration exhibits better polarization selectivity compared to the Ti-Si-Ti configuration. When the TE wave is incident, due to $n_{Si} < \sqrt{n_{Al}}$, Eq. (5) does not fit here and a F-P mode was excited at the wavelength of 9.1μm. Compared with the Ti-Si-Ti configuration, mode 3 has a blue shift of 0.9 μm, and the absorption rate of mode 3 drops to 15%. The absorption rate in the wavelength band away from the absorption peak also drops below 5% due to the low lossy of Al. In the wavelength range of 7.5~13.5μm, the average absorption rate reached 91.7%, the absorption rates of mode1 and mode2 reached 99.9% and 93.7%, respectively. We also noticed that the absorption peaks corresponding to the mode1 and mode2 respectively blue shifted to 8.15μm and 12.3μm. The wavelength shift of mode1 can be explained by the excitation formula of PSPR [47]:$k_{PSP} = \frac{\omega}{c}\sqrt{\frac{\varepsilon_m \varepsilon_d}{\varepsilon_m + \varepsilon_d}}$. Since $\varepsilon_{Al} > \varepsilon_{Ti}$ in the simulated wavelength band, the absorption peak caused by PSPR blue shift from 8.6μm to 8.15μm. The change in permittivity of the bottom also reduced the inductance of the bottom (L_b), result in a blue shift of mode2 from 12.9μm to12.3μm.

We have also calculated the equivalent impedance of the absorber under the incident TM and TE waves. As shown in Fig. 3(c), under the incident TM wave, the absorber maintains impedance matching over a wide spectrum. The impedances at the absorption peaks in mode1 and mode2 are Z_1=0.9+i0.09, Z_2=0.9-i0.1. Under the incident TE wave, although there is still the imaginary part of the impedance reaches zero at the wavelength of 9.9 μm, the real part reaches 5, which is very different from the air impedance and the absorption rate drops to 15%. As shown in Fig. 3(b), the solid line represents the energy absorption of each layer when the TM wave is incident. It can be seen that 90% of the incident light energy is absorbed by the resonator layer, and the absorption contribution of the dielectric layer and the bottom layer are both less than 5%. The dotted line represents the energy absorption of each layer under the incident TE wave. The energy is mainly concentrated in the bottom, and the absorption rate at mode3 drops below 15%, due to the low loss of aluminum.

In the range of simulated waveband, the maximum value of the extinction ratio defined as $\eta = A_{TM}/A_{TE}$ reached 24, and the average value was 11.34 (Fig. 3(d)). Compared with the Ti-Si-Ti configuration, the extinction ratio increased by about 5 times. Since all the absorption of incident TE waves comes from the aluminum bottom, it can be replaced with lower loss metals such as gold and silver to further reduce the absorption of TE waves and obtain a higher extinction ratio. It is worth mentioning that if we only consider the effective absorption, that is,

Optics EXPRESS

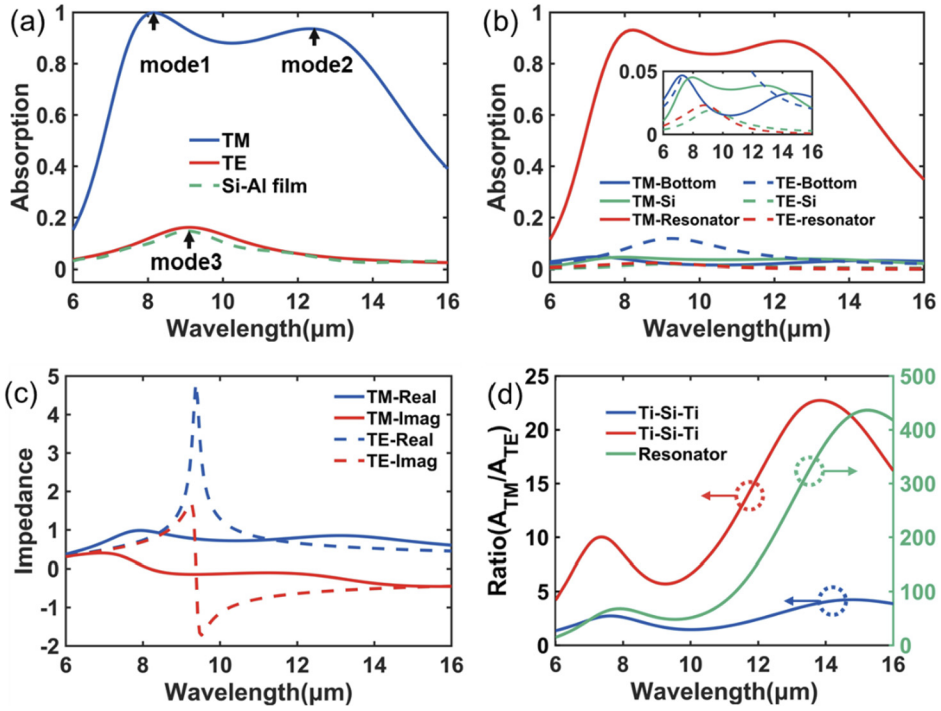

Fig. 3. (a) The absorption spectrum of the absorber under TM and TE incidence and the absorption spectrum of the Si-Al film. (b) The absorption of each component of the absorber when TM (solid line) and TE (dashed line) are incidents, the inset is enlarged view of the absorption spectrum for the bottom and Si. (c) The equivalent impedance of the absorber under incident of TM wave (solid line) and TE wave (dashed line). (d) The extinction ratio of the Ti-Si-Ti configuration and the Ti-Si-Al configuration, and the extinction ratio of the resonator in the Ti-Si-Al configuration.

the absorption in the resonator layer. The value of the extinction ratio in the simulated waveband can be as high as 436, the minimum value is 50, and the average value is reached 125.

2.3. *Polarization insensitive and incident angle insensitive spatially concentrated broadband absorption*

For some applications such as thermal harvesting, cloak, and microbolometers, broadband, polarization insensitive and incident angle insensitive absorption are required. Following we will certify that by adopting a rotationally symmetrical resonator, we can achieve wide-angle and polarization-insensitive spatially concentrated broadband absorption. As shown in Fig. 4(a), we changed the resonator to a cross with 90° rotational symmetry. According to the previous analysis, a broadband absorption can be obtained when the cut-wire is parallel to the incident electric field component, and when the cut-wire is perpendicular to the incident electric field component, there is no SPR in the simulated wavelength band. That is, the cross resonator can be treated as a pair of cut-wires perpendicular to each other so that the same "cut-wire" resonator couple with the TM and TE waves and a polarization-insensitive broadband absorption can be obtained. Figure 4(c) shows the absorption spectrum of the absorber and the absorption contribution of each component. It can be seen that the average absorption rate of the absorber in the 7.5~13.25μm wavelength range reaches 94%. The absorption rates at 8.1μm and 12.2μm reached 98.6% and 97.4%, respectively. Correspondingly, the absorber also shows excellent

Optics EXPRESS

spatially concentrated absorption, 90% of the incident light is absorbed by the cross resonator, and as shown in the insert view of Fig. 4(c), the absorption contribution of the bottom and the dielectric layer is less than 5%. As shown in Fig. 5(b), we plotted the thermal distribution of the resonator-dielectric interface in the condition of TM wave incident, at the two absorption peaks, respectively. The different colors in the figure represent the gradient of the normalized energy intensity after taking the logarithm. It can be seen that the thermal is concentrated in the resonator and mainly focused on the axis parallel to the incident electric field component. The spatially concentrated absorption is conducive to creating local hot spots to generate hot electrons with higher energy than free electrons, which can be used in hot-electron devices to improve their performance.

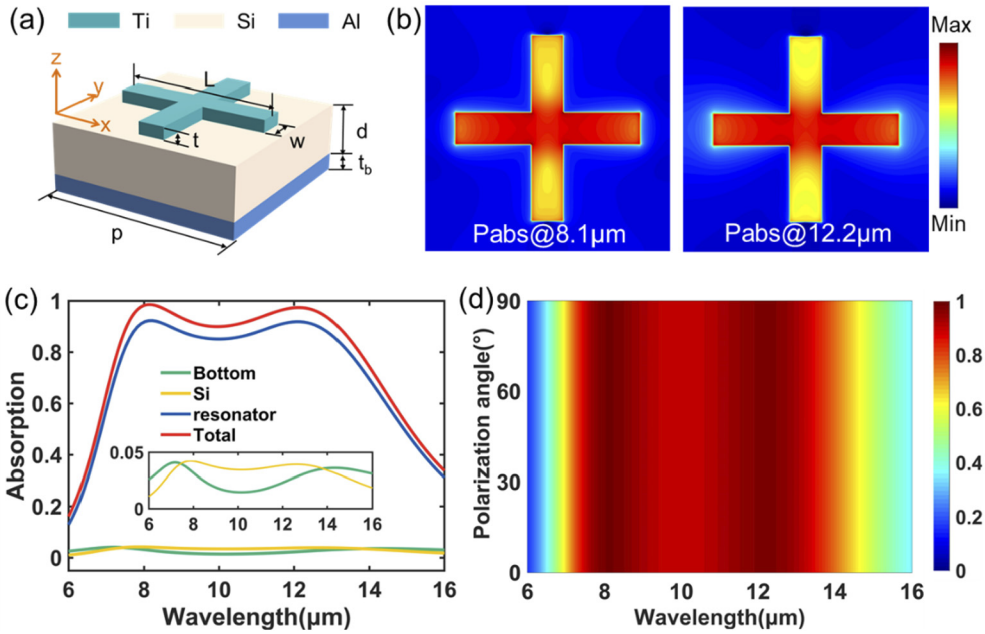

Fig. 4. (a) Schematic diagram of the polarization-insensitive broadband absorber. (b) The thermal distribution at the absorption peak at the resonator-dielectric interface. (c) The absorption spectrum and absorption of each component of the polarization-insensitive broadband absorber, the inset is enlarged view of the absorption spectrum for the bottom and Si, (d) The dependence on the polarization angle of the performance of the polarization-insensitive broadband absorber.

To verify the polarization characteristics of the absorber, we calculated the absorption spectrum with a polarization angle of 0–90° by scanning at each step of 10°, as shown in Fig. 4(d). When the polarization angle changed from 0° to 90°, the absorption spectrum did not change. To characterize the dependence of the absorber's performance on the incident angle, we carried out a scanning simulation with the step length as 10° under the incident TM and TE waves, and the results are shown in Fig. 5. It can be seen that when the incident angle of the TM wave reaches 60°, the absorber still maintains more than 90% absorption (Fig. 5(a)). For TE waves, the left peak still maintains an absorption rate of more than 90% when the incident angle reaches 60°, while the absorption rate of the right peak gradually decreases as the incident angle increases and drops to 73% as the incident angle reaches 60° (Fig. 5(b)). This is because the electric field component incident on the surface of the resonator decreases as the incident angle increases, resulting in a decrease in the intensity of the LSPR. Nevertheless, the average absorption rate of TE wave in the wavelength range of 8~14μm remains above 70%, and the absorption rate of unpolarized

Optics EXPRESS

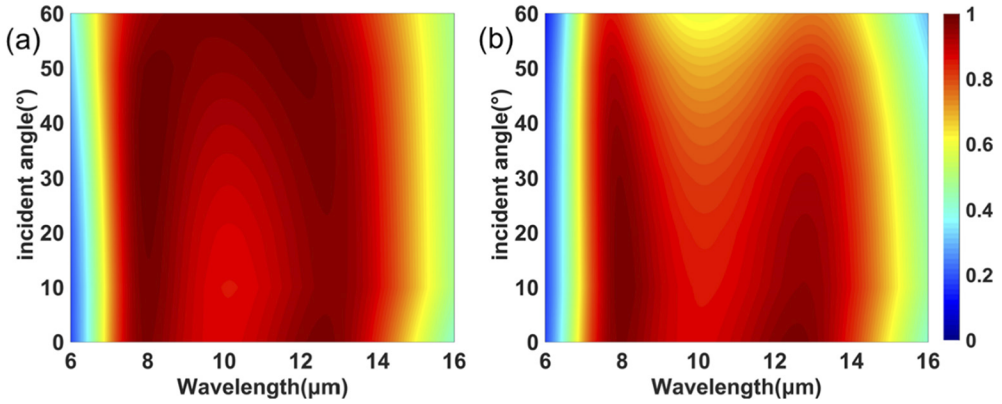

Fig. 5. The dependence of the absorber's performance on the incident angle (a) TM incident (b) TE incident.

light remains above 85% when the incident angle reaches 60°. Therefore, polarization insensitive and incident angle insensitive spatially concentrated broadband absorption is obtained by the cross-shaped resonator configuration absorber.

3. Conclusion

In summary, we proposed a long-wave infrared spatially concentrated broadband absorber design with a simple configuration. First, we proposed a cut-wire Ti-Si-Ti configuration, which realized the broadband absorption of TM wave and the single-peak absorption of TE wave. The transmission line analysis indicated that the absorber match impedance with the air in a wide waveband range in the case of TM wave incidence, and mismatch impedance in the case of TE wave incidence. Field distribution analysis indicated that the broadband absorption of TM comes from the SPRs excited by the resonator, while the absorption of TE waves comes from the cavity mode. Since the absorption of the incident TE wave mainly comes from the intrinsic absorption of the titanium bottom, we replaced the bottom metal with the low-loss metal aluminum to obtain polarization-selective broadband absorption. The absorption of the TE wave drops below 15%, while the average absorption rate of the TM wave reaches 91.7% in the 7.5~13.25μm wavelength range, so the average extinction ratio of 11.34 is obtained. Moreover, more than 90% of the incident light is absorbed by the resonator, showing the characteristics of spatial concentration, and the effective extinction ratio of the resonator reaches 125. Finally, we use a cross resonator which can be treated as a pair of cut-wires perpendicular to each other to obtain polarization-insensitive spatially concentrated broadband absorption, the average absorption rate of the absorber in the wavelength range of 7.5~13.25μm reaches 94% under normal incidence. In the case of oblique incidence, when the incident angle reaches 60°, TM and TE waves maintain 90% and 70% absorption respectively, and the absorption of unpolarized light reaches 80%. The absorber we designed can be used for hot-electron devices, infrared imaging, thermal detection, and other devices.

Funding. National Natural Science Foundation of China (61735018, 61805242); Jilin Scientific and Technological Development Program (20190103014JH); Excellent Member of Youth Innovation Promotion Association of the Chinese Academy of Sciences (2014193, Y201836); Leading Talents and Team Project of Scientific and Technological Innovation for Young and Middle-aged Groups in Jilin Province (20190101012JH); Project of CIOMP-Duke Collaborative Research (201903002); CAS President's International Fellowship Initiative (PIFI).

Disclosures. The authors declare no conflicts of interest.

Optics EXPRESS

Data availability. Data underlying the results presented in this paper are not publicly available at this time but may be obtained from the authors upon reasonable request.

References

1. N. Liu, M. Mesch, T. Weiss, M. Hentschel, and H. Giessen, "Infrared perfect absorber and its application as plasmonic sensor," Nano Lett. **10**(7), 2342–2348 (2010).
2. Z. Qian, S. Kang, V. Rajaram, C. Cassella, N. E. McGruer, and M. Rinaldi, "Zero-power infrared digitizers based on plasmonically enhanced micromechanical photoswitches," Nat. Nanotechnol. **12**(10), 969–973 (2017).
3. A. Carrara, N. Maccaferri, A. Cerea, A. Bozzola, F. De Angelis, R. Proietti Zaccaria, and A. Toma, "Plasmon Hybridization in Compressible Metal–Insulator–Metal Nanocavities: An Optical Approach for Sensing Deep Sub-Wavelength Deformation," Advanced Optical Materials 8(2020).
4. U. T. D. Thuy, N. T. Thuy, N. T. Tung, E. Janssens, and N. Q. Liem, "Large-area cost-effective lithography-free infrared metasurface absorbers for molecular detection," APL Materials 7(2019).
5. A. Lochbaum, Y. Fedoryshyn, A. Dorodnyy, U. Koch, C. Hafner, and J. Leuthold, "On-Chip Narrowband Thermal Emitter for Mid-IR Optical Gas Sensing," ACS Photonics **4**(6), 1371–1380 (2017).
6. A. Shahsafi, G. Joe, S. Brandt, A. V. Shneidman, N. Stanisic, Y. Xiao, R. Wambold, Z. Yu, J. Salman, J. Aizenberg, and M. A. Kats, "Wide-Angle Spectrally Selective Absorbers and Thermal Emitters Based on Inverse Opals," ACS Photonics **6**(11), 2607–2611 (2019).
7. L. Zhou, Y. Tan, D. Ji, B. Zhu, P. Zhang, J. Xu, Q. Gan, Z. Yu, and J. Zhu, "Self-assembly of highly efficient, broadband plasmonic absorbers for solar steam generation," Sci. Adv. **2**(4), e1501227 (2016).
8. C. Fei Guo, T. Sun, F. Cao, Q. Liu, and Z. Ren, "Metallic nanostructures for light trapping in energy-harvesting devices," Light: Sci. Appl. **3**(4), e161 (2014).
9. Y. Zhai, Y. Ma, S. N. David, D. Zhao, R. Lou, G. Tan, R. Yang, and X. Yin, "Scalable-manufactured randomized glass-polymer hybrid metamaterial for daytime radiative cooling," Science **355**(6329), 1062–1066 (2017).
10. K. Sun, C. A. Riedel, Y. Wang, A. Urbani, M. Simeoni, S. Mengali, M. Zalkovskij, B. Bilenberg, C. H. de Groot, and O. L. Muskens, "Metasurface Optical Solar Reflectors Using AZO Transparent Conducting Oxides for Radiative Cooling of Spacecraft," ACS Photonics **5**(2), 495–501 (2018).
11. N. I. Landy, S. Sajuyigbe, J. J. Mock, D. R. Smith, and W. J. Padilla, "Perfect metamaterial absorber," Phys. Rev. Lett. **100**(20), 207402 (2008).
12. H. R. Seren, J. Zhang, G. R. Keiser, S. J. Maddox, X. Zhao, K. Fan, S. R. Bank, X. Zhang, and R. D. Averitt, "Nonlinear terahertz devices utilizing semiconducting plasmonic metamaterials," Light: Sci. Appl. **5**(5), e16078 (2016).
13. W. Li and J. Valentine, "Metamaterial perfect absorber based hot electron photodetection," Nano Lett. **14**(6), 3510–3514 (2014).
14. H. Cai, Y. Sun, X. Wang, and S. Zhan, "Design of an ultra-broadband near-perfect bilayer grating metamaterial absorber based on genetic algorithm," Opt. Express **28**(10), 15347–15359 (2020).
15. A. Lochbaum, A. Dorodnyy, U. Koch, S. M. Koepfli, S. Volk, Y. Fedoryshyn, V. Wood, and J. Leuthold, "Compact Mid-Infrared Gas Sensing Enabled by an All-Metamaterial Design," Nano Lett. **20**(6), 4169–4176 (2020).
16. X. Tan, H. Zhang, J. Li, H. Wan, Q. Guo, H. Zhu, H. Liu, and F. Yi, "Non-dispersive infrared multi-gas sensing via nanoantenna integrated narrowband detectors," Nat. Commun. **11**(1), 5245 (2020).
17. K. T. Lin, H. Lin, T. Yang, and B. Jia, "Structured graphene metamaterial selective absorbers for high efficiency and omnidirectional solar thermal energy conversion," Nat. Commun. **11**(1), 1389 (2020).
18. Y. Li, D. Li, D. Zhou, C. Chi, S. Yang, and B. Huang, "Efficient, Scalable, and High-Temperature Selective Solar Absorbers Based on Hybrid-Strategy Plasmonic Metamaterials," Solar RRL 2(2018).
19. C. C. Chang, W. J. M. Kort-Kamp, J. Nogan, T. S. Luk, A. K. Azad, A. J. Taylor, D. A. R. Dalvit, M. Sykora, and H. T. Chen, "High-Temperature Refractory Metasurfaces for Solar Thermophotovoltaic Energy Harvesting," Nano Lett. **18**(12), 7665–7673 (2018).
20. B. Zeng, Z. Huang, A. Singh, Y. Yao, A. K. Azad, A. D. Mohite, A. J. Taylor, D. R. Smith, and H. T. Chen, "Hybrid graphene metasurfaces for high-speed mid-infrared light modulation and single-pixel imaging," Light: Sci. Appl. **7**(1), 51 (2018).
21. K. Fan, J. Y. Suen, X. Liu, and W. J. Padilla, "All-dielectric metasurface absorbers for uncooled terahertz imaging," Optica 4(2017).
22. W. Ma, Y. Wen, X. Yu, Y. Feng, and Y. Zhao, "Performance enhancement of uncooled infrared focal plane array by integrating metamaterial absorber," Applied Physics Letters 106(2015).
23. A. Tittl, A. K. Michel, M. Schaferling, X. Yin, B. Gholipour, L. Cui, M. Wuttig, T. Taubner, F. Neubrech, and H. Giessen, "A Switchable Mid-Infrared Plasmonic Perfect Absorber with Multispectral Thermal Imaging Capability," Adv. Mater. **27**(31), 4597–4603 (2015).
24. H. X. Xu, G. Hu, Y. Wang, C. Wang, M. Wang, S. Wang, Y. Huang, P. Genevet, W. Huang, and C. W. Qiu, "Polarization-insensitive 3D conformal-skin metasurface cloak," Light Sci Appl **10**(1), 75 (2021).
25. J. Zhou, A. F. Kaplan, L. Chen, and L. J. Guo, "Experiment and Theory of the Broadband Absorption by a Tapered Hyperbolic Metamaterial Array," ACS Photonics **1**(7), 618–624 (2014).
26. K. Üstün and G. Turhan-Sayan, "Wideband long wave infrared metamaterial absorbers based on silicon nitride," Journal of Applied Physics 120(2016).

Optics EXPRESS

27. Y. Zhou, Z. Liang, Z. Qin, E. Hou, X. Shi, Y. Zhang, Y. Xiong, Y. Tang, Y. Fan, F. Yang, J. Liang, C. Chen, and J. Lai, "Small-sized long wavelength infrared absorber with perfect ultra-broadband absorptivity," Opt. Express **28**(2), 1279–1290 (2020).
28. Y. Zhou, Z. Liang, Z. Qin, X. Shi, D. Meng, L. Zhang, and X. Wang, "Broadband long wavelength infrared metamaterial absorbers," Results in Physics 19(2020).
29. H. F. Wang, J. X. Shi, L. Y. Qian, C. C. Yan, C. Q. Han, and Y. P. Zhao, "Large-area broadband optical absorber fabricated by shadowing sphere lithography," Opt. Express **26**(6), 7507–7515 (2018).
30. R. Contractor, G. D'Aguanno, and C. Menyuk, "Ultra-broadband, polarization-independent, wide-angle absorption in impedance-matched metamaterials with anti-reflective moth-eye surfaces," Opt. Express **26**(18), 24031–24043 (2018).
31. N. T. Q. Hoa, P. H. Lam, P. D. Tung, T. S. Tuan, and H. Nguyen, "Numerical Study of a Wide-Angle and Polarization-Insensitive Ultrabroadband Metamaterial Absorber in Visible and Near-Infrared Region," IEEE Photonics J. **11**(1), 1–8 (2019).
32. K. Dixon, A. O. Montazeri, M. Shayegannia, E. S. Barnard, S. Cabrini, N. Matsuura, H. Y. Holman, and N. P. Kherani, "Tunable rainbow light trapping in ultrathin resonator arrays," Light: Sci. Appl. **9**(1), 194 (2020).
33. W. W. Zhang, H. Qi, A. T. Sun, Y. T. Ren, and J. W. Shi, "Periodic trapezoidal VO2-Ge multilayer absorber for dynamic radiative cooling," Opt. Express **28**(14), 20609–20623 (2020).
34. B. M. Adomanis, C. M. Watts, M. Koirala, X. Liu, T. Tyler, K. G. West, T. Starr, J. N. Bringuier, A. F. Starr, N. M. Jokerst, and W. J. Padilla, "Bi-layer metamaterials as fully functional near-perfect infrared absorbers," Applied Physics Letters 107(2015).
35. K. Üstün and G. Turhan-Sayan, "Broadband LWIR and MWIR metamaterial absorbers with a simple design topology: almost perfect absorption and super-octave band operation in MWIR band," J. Opt. Soc. Am. B 34(2017).
36. K. Yang, J. Wang, X. Yao, D. Lyu, J. Zhu, Z. Yang, B. Liu, and B. Ren, "Large-Area Plasmonic Metamaterial with Thickness-Dependent Absorption," Advanced Optical Materials 9(2020).
37. F. Ding, J. Dai, Y. Chen, J. Zhu, Y. Jin, and S. I. Bozhevolnyi, "Broadband near-infrared metamaterial absorbers utilizing highly lossy metals," Sci Rep **6**(1), 39445 (2016).
38. A. Kadambi, V. Taamazyan, B. Shi, and R. Raskar, "Polarized 3D: High-Quality Depth Sensing with Polarization Cues," in *2015 IEEE International Conference on Computer Vision (ICCV)*, 2015), 3370–3378.
39. Yan-Lin Liao and Yan Zhao, "A wide-angle broadband polarization-dependent absorber with stacked metal-dielectric grating," Opticsunications (2016).
40. K. Zhou, Q. Cheng, L. Lu, B. Li, J. Song, and Z. Luo, "Dual-band tunable narrowband near-infrared light trapping control based on a hybrid grating-based Fabry-Perot structure," Opt. Express **28**(2), 1647–1656 (2020).
41. J. Jeong, D. Kim, M. Seo, and D. S. Kim, "Strongly Localized ohmic Absorption of Terahertz Radiation in Nanoslot Antennas," Nano Lett. **19**(12), 9062–9068 (2019).
42. A. Sobhani, M. W. Knight, Y. Wang, B. Zheng, N. S. King, L. V. Brown, Z. Fang, P. Nordlander, and N. J. Halas, "Narrowband photodetection in the near-infrared with a plasmon-induced hot electron device," Nat. Commun. **4**(1), 1643 (2013).
43. Z. Li, L. Stan, D. A. Czaplewski, X. Yang, and J. Gao, "Wavelength-selective mid-infrared metamaterial absorbers with multiple tungsten cross resonators," Opt. Express **26**(5), 5616–5631 (2018).
44. A. D. Rakić, A. B. Djurišić, J. M. Elazar, and M. L. Majewski, "Optical properties of metallic films for vertical-cavity optoelectronic devices," Appl. Opt. **37**(22), 5271–5283 (1998).
45. F. Gervais, "Handbook of Optical Constants of Solids ii," (1985).
46. A. Tittl, M. G. Harats, R. Walter, X. Yin, M. Schäferling, N. Liu, R. Rapaport, and H. Giessen, "Quantitative Angle-Resolved Small-Spot Reflectance Measurements on Plasmonic Perfect Absorbers: Impedance Matching and Disorder Effects," ACS Nano **8**(10), 10885–10892 (2014).
47. C. Genet and T. W. Ebbesen, "Light in tiny holes," Nature **445**(7123), 39–46 (2007).
48. Y. Q. Ye, Y. Jin, and S. He, "Omnidirectional, polarization-insensitive and broadband thin absorber in the terahertz regime," J. Opt. Soc. Am. B **27**(3), 498–504 (2010).
49. M. ElKabbash, S. Iram, T. Letsou, M. Hinczewski, and G. Strangi, "Designer Perfect Light Absorption Using Ultrathin Lossless Dielectrics on Absorptive Substrates," Adv. Opt. Mat. **6**, 180067 (2018).